**RESEARCH ARTICLE**

**Key Points:**
- The observed long-lasting banded convective activity and associated mesoscale gravity waves were simulated reasonably well by WRF
- Analyses show that both wave ducting and wave-convection interaction may be responsible for the propagating and maintenance of the mesoscale gravity waves
- The mesoscale gravity wave characteristics are likely to be jointly determined by the low-level ducting stable layer properties and the life cycle of attendant moist convection

**Correspondence to:**
Y. Du and F. Zhang,
duyu7@mail.sysu.edu.cn;
fzhang@psu.edu

**Author Contributions:**
**Conceptualization:** Yu Du, Fuqing Zhang
**Data curation:** Yu Du
**Formal analysis:** Yu Du
**Funding acquisition:** Yu Du
**Investigation:** Yu Du, Fuqing Zhang
**Methodology:** Yu Du, Fuqing Zhang
**Resources:** Yu Du
**Validation:** Yu Du
**Visualization:** Yu Du
**Writing - original draft:** Yu Du
**Writing – review & editing:** Yu Du, Fuqing Zhang

# Banded Convective Activity Associated With Mesoscale Gravity Waves Over Southern China

**Yu Du[1]** (iD) **and Fuqing Zhang[2]** (iD)

[1]Center for Monsoon and Environment Research, School of Atmospheric Sciences, and Guangdong Province Key Laboratory for Climate Change and Natural Disaster Studies, Sun Yat-sen University, Guangzhou, China, [2]Department of Meteorology and Atmospheric Science, and Center for Advanced Data Assimilation and Predictability Techniques, Pennsylvania State University, University Park, PA, USA

**Abstract** Banded convective activity that occurred near the south coast of China on 30 January 2018 was investigated through convection-allowing simulations using a nonhydrostatic mesoscale model. The simulations capture reasonably well the observed characteristics of this event. The convective bands are found to be closely related to an episode of mesoscale gravity waves propagating northeastward with a wave speed of around 12 m/s and a primary wavelength of about ~40–50 km. Further analyses and sensitivity experiments reveal that the environment provides a wave duct for these gravity waves, with a thick low-level stable layer below 850 hPa capped by a low-stability reflecting layer with a critical level. The strength and depth of the low-level stable layer determine the intrinsic phase speed and wavelength of the ducted gravity waves. In the sensitivity tests that the stable layer depth is reduced, the wave characteristics change according to what are predicted with the wave duct theory. The convective bands collocate and propagate in phase with the peak updraft regions of the gravity waves, suggesting strong interactions of convection and gravity waves, in which the ducted gravity waves can trigger and modulate convection, while latent heating from convection enhances the waves. In essence, both wave ducting and wave-convection interaction are jointly responsible for the banded convective activity.

## 1. Introduction

Gravity waves are ubiquitous phenomenon observed in the atmosphere with an extensive range of wavelengths, periods, and phase speeds (Nappo, 2002). They are related to the disturbances in surface pressure, winds, and also convective activities (Koch et al., 1988; Ralph et al., 1993; Uccellini & Koch, 1987). Previous studies have documented that gravity waves can be generated by mountains, shear instability, front/jets, and convection (e.g., Fritts & Alexander, 2003; Kruse & Smith, 2015; Lane, 2015; Li & Chen, 2017; Liu et al., 2018; Plougonven & Zhang 2015; Wang & Zhang, 2007; Wang et al., 2009, 2018; Zhang, 2004; Zhang & Koch, 2000). Gravity waves have many impacts on the atmosphere such as through distribution of free troposphere temperature in tropics and the circulation-convection interaction (Wang et al., 2013; Wang & Sobel, 2011). Convection might exhibit wave features such as wavelike banded convection when convection is coupled with mesoscale gravity waves (Lane & Zhang, 2011; Raymond, 1987) that can sometimes persist in the low-level wave duct (Lindzen & Tung, 1976; Powers & Reed, 1993; Zhang et al., 2001).

Gravity waves may impact the formation and development of convection (Adams-Selin & Johnson 2013; Lac et al., 2002; Schmidt & Cotton, 1990; Stobie et al., 1983; Su & Zhai, 2017; Uccellini & Koch, 1987; Wilson et al., 2018; Zhang et al., 2001) and the cloud environment (Lane & Reeder, 2001). They can organize convection into wave trains (Liu & Moncrieff, 2004; Tulich & Mapes, 2008). Uccellini (1975) suggested that gravity waves not only excite new convection but also enhance the existing convective elements along the wave path since gravity waves with a sufficiently large amplitude could lead to moist air condensation (Einaudi & Lalas, 1973). Convection is also an important source of gravity waves (Alexander et al., 1995; Bosart & Cussen, 1973; Lin & Goff, 1988; Stephan et al., 2016). Fovell et al. (2006) found that simulated gravity waves of both low and high frequencies are generated in response to latent heating of the parent storm and subsequently propagate away and ahead of the storm. Convection and gravity waves are known to couple and interact synergistically (Cram et al., 1992; Lane & Zhang, 2011; Miller & Sanders, 1980; Powers & Reed, 1993; Raymond, 1987; Ruppert & Bosart, 2014; Zhang et al., 2001) through a mechanism commonly referred to as "wave-CISK (convective instability of the second kind)."
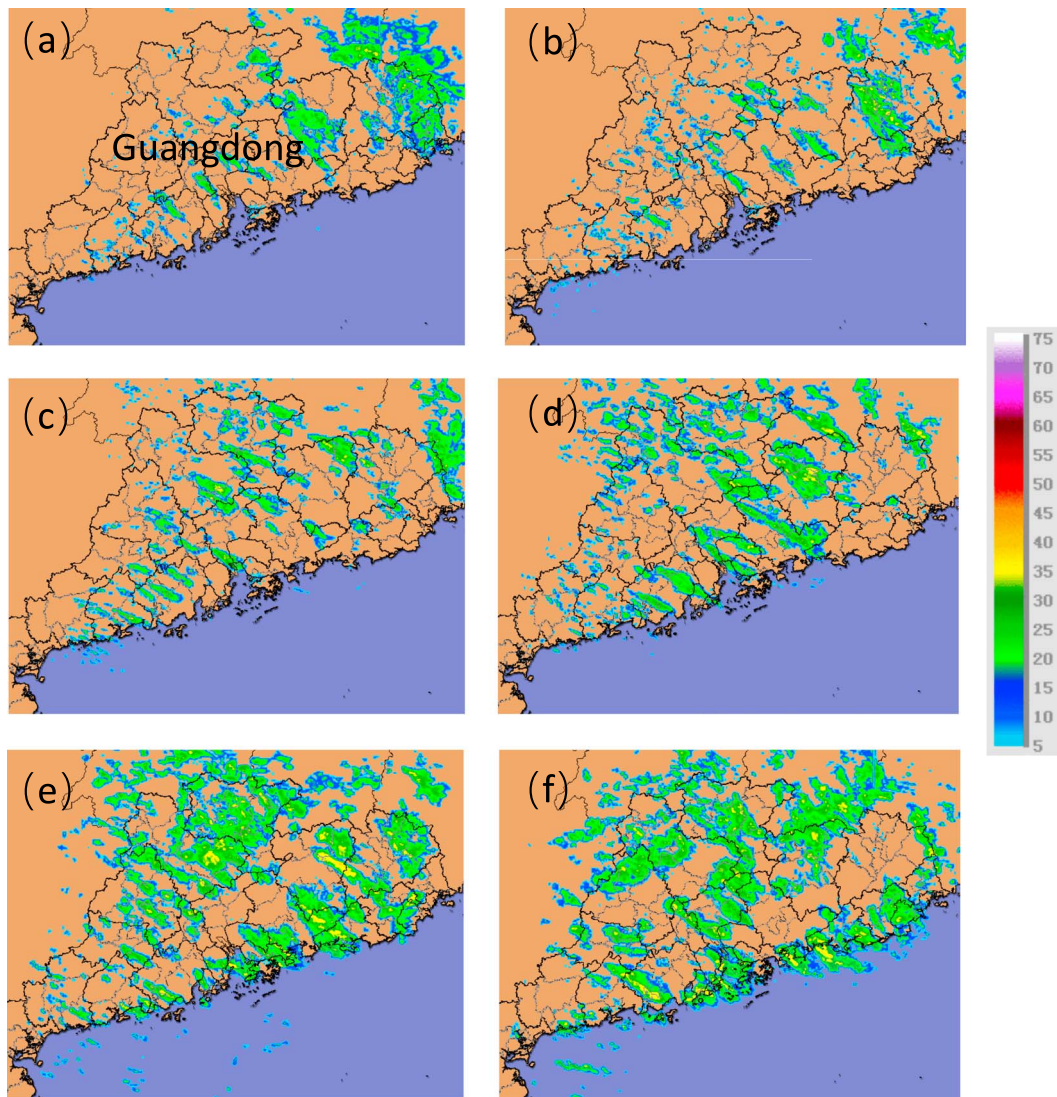
**Figure 1.** Radar composite reflectivity derived from operational weather radars in Guangdong Province on (a) 0800, (b) 1000, (c) 1200, (d) 1400, (e) 1600, and (f) 1800 UTC 30 January 2018.

The wave-CISK concept was originally proposed by Lindzen (1974) and Raymond (1975) in which gravity waves produce low-level convergence while the gravity waves may respond positively to the latent heating associated with the resulting convection. Koch et al. (1988) inherited the same terminology (wave-CISK) but stressed more the positive feedback process between gravity waves and convection: latent heating from convection generates and enhances gravity waves which in turn initiate and organize convection. The terminology "wave-CISK" has since evolved into a broader concept that describes the coupling between gravity waves and convection (Powers, 1997; Zhang et al., 2001).

Long-lived gravity waves can propagate horizontally in a wave duct (Eom, 1975; Nappo, 2002). Lindzen and Tung (1976) conceptualized that the ducted gravity waves propagate in a low-level stable layer that is overlaid by a reflecting layer which has low stability and contains a critical level. Such an environment can support and maintain gravity waves near the surface for long duration without significant loss of energy (Zhang & Koch, 2000). As the waves propagate through the critical level, the wave energy is extracted from the basic flow when the Richardson number is less than 1/4; otherwise, the wave energy will be absorbed at the critical level (Booker & Bretherton, 1967; Jones, 1968; Rosenthal & Lindzen,
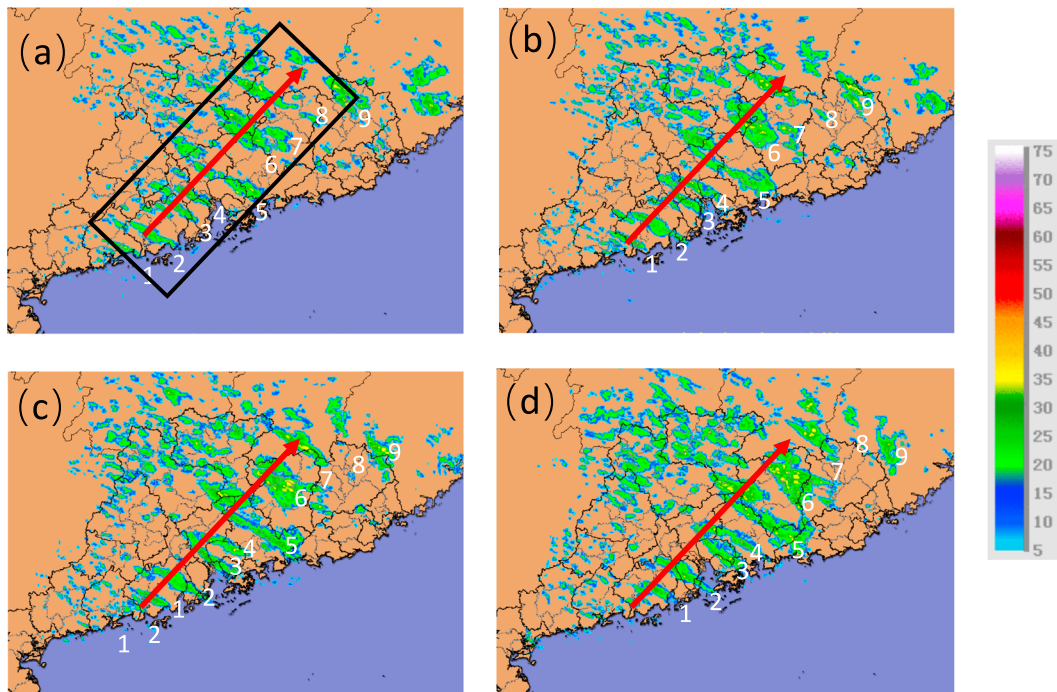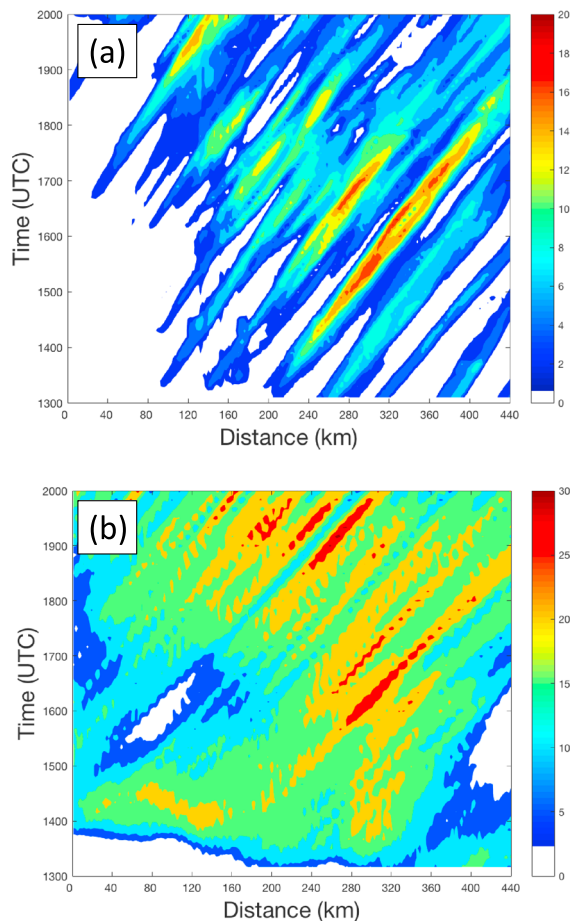
**Figure 2.** Radar composite reflectivity derived from operational weather radars in Guangdong Province on (a) 1300, (b) 1330, (c) 1400, and (d) 1430 UTC 30 January 2018. The red arrows indicate the moving direction of the convective bands, and the white numbers mark individual convective bands.

1983). The wave ducting theory has been widely used to explain long-lived gravity wave events in observational studies (Bosart et al., 1998; Koch et al., 1988; Kusunoki et al., 2000; Ralph et al., 1993) and numerical simulations (Crook, 1988; Liu et al., 2018; Powers, 1997; Powers & Reed, 1993; Zhang et al., 2001).

Some studies suggested that the coexistence of wave-CISK (wave-convection interaction) and wave ducting (Koch et al., 2001; Powers & Reed, 1993; Zhang et al., 2001), or the "ducted wave-CISK," could explain the propagation and maintenance of wavelike convective bands associated with gravity waves. Localized convection traveling with gravity waves supplies energy and amplifies the waves, which can compensate the vertical propagation of wave energy in the nonperfect wave duct (Zhang et al., 2001).

On 30 January 2018, an episode of wavelike banded convective activity potentially associated with mesoscale gravity waves was observed through the operational radar's mosaic images over Guangdong Province in South China. These convective bands propagated horizontally for long distances and maintained a coherent wavelike structure for approximately 10 hr. The purpose of the present study is to explore the characteristics and potential dynamical mechanisms of the banded convection and the associated gravity waves during this event. We seek to answer the following interesting questions: (1) why did the wavelike pattern of convection persist for a long time? (2) What factors determine the phase speed and wavelength of the gravity waves, as well as the scales of the wavelike convective bands? (3) What is the role of convection in the development of gravity waves?

We will use both observational data and convective-permitting mesoscale simulations to investigate the main features and dynamics of the banded convective activity. In section 2, the episode of banded convective activity is introduced with respect to its evolution and relevant synoptic background. Section 3 describes the model configurations used and sensitivity experiments designed in this study. The comparison between model simulations and observation is also conducted in section 3. The potential mechanisms of wave ducting and wave-convection interaction are discussed in section 4. The results are summarized in section 5.

**Figure 3.** Distance-time Hovmöller diagrams of radar composite reflectivity compositing along the wavefronts in the black box of Figures 2a and 6d from the (a) observation and (b) control run. The left (right) side of x axis is southwest (northeast) side of boxes.

## 2. Case Overview

Figure 1 shows the evolution of the radar composite reflectivity (mosaic) derived from the operational weather radar network in Guangdong Province (indicated by the black outline) during 0800–1800 UTC 30 January 2018. The northwest-southeast oriented banded convection was evident covering nearly the entire Guangdong Province and exhibited wave features, which lasted for nearly 10 hr. At around 1400 UTC (Figure 1d), the wave signal became most significant. At least nine convective bands moved coherently northeastward. As shown in Figure 2, the long-dimensional horizontal extent of individual convective bands varied from 100 to 300 km, while their horizontal spacing distance was around 50 km. To illustrate the detailed propagation and evolution of those convective bands, a distance-time Hovmöller diagram of radar composite reflectivity compositing along the wavefronts in the black box of Figure 2a is shown in Figure 3a. It clearly shows that the propagation speed of the convective bands was around 12 m/s. These convective bands exhibited characteristics of northeastward propagating mesoscale waves featuring a primary horizontal wavelength of around 50 km and a wave period of about 1 hr.

In order to show the synoptic background circulation and environment in this event, the National Centers for Environmental Prediction Final Operational Global Analysis data is analyzed as shown in Figure 4, which presents weather variables at different levels at 1200 UTC 30 January 2018 when the banded convective activity was evident. A westerly jet at 500 hPa (exceeding 30 m/s) was located at latitude of around 25°N (Figure 4a). A northeast-southwest oriented shear line at 850 hPa (indicated by a red line in Figure 4b) existed near the north edge of Guangdong Province accompanied by a large gradient zone of equivalent potential temperature (Figure 4b). The southerly (northeasterly) winds prevailed at 850 hPa (950 hPa) over Guangdong, and correspondingly, the vertical wind shear was evident at low levels (Figures 4b and 4c). The atmosphere at 950 hPa was moist and saturated (Figure 4c). This event was affected by a cold front along the coast region, and the banded activity was located in the cold side (Figure 4d). Next, we will explore in detail the environment and possible mechanisms which support the banded convective activity using cloud-permitting numerical simulations.

## 3. Model Simulation

### 3.1. Model Configuration

For the sake of understanding the thermal and dynamical mechanisms of the banded convective activity, the Advanced Research Weather Research and Forecasting model (Skamarock et al., 2005) is utilized in the present study. Given the sensitivity to initial conditions and model resolution and physics (Zhang et al., 2003), along with limited predictability at the mesoscales (Sun & Zhang, 2016), it is often difficult for mesoscale models to precisely simulate gravity waves and their interaction with convection (Du & Chen, 2019; Zhang et al., 2003). By conducting multiple experiments, the control run initialized at 1200 UTC 30 January 2018 is selected that can capture reasonably well the episode of banded convective activities. It is noted that the simulations' capability is highly sensitive to the initial conditions. Neither of simulations initiated at 0000 or 0600 UTC 30 January simulated the convective bands well, especially the orientations of the bands (not shown). The control run and other sensitivity simulations use a one-way nested grid setup with three domains (D01, D02, and D03; Figure 5), of which the horizontal grid spacing are 9, 3, and 1 km, respectively. The horizontal resolution of the inner domain (1 km) is sufficient to revolve the gravity waves with horizontal wavelengths of ~20–50 km in this case. The vertical grid contains 51 levels with the model top of 50 hPa where the absorbing layer of gravity waves is used. The Final analysis is used as the initial and
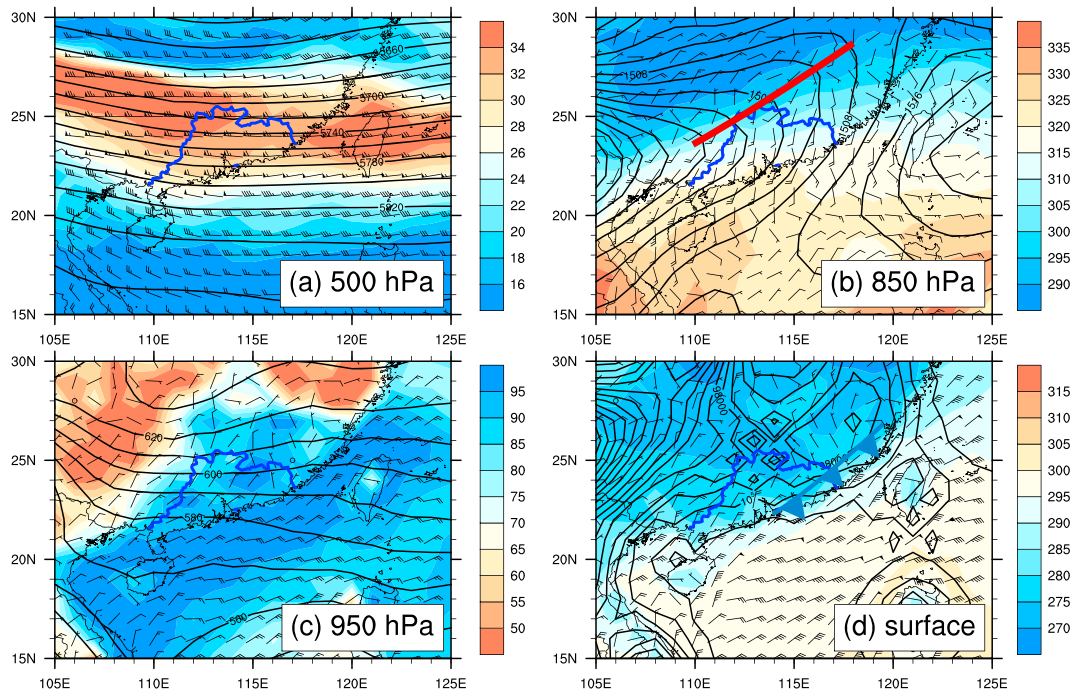
**Figure 4.** NCEP FNL (final) operational global analysis data at 1200 UTC 30 January 2018 showing (a) the geopotential height (gpm; contour), wind speed (m/s; shading), and superimposed with horizontal wind barbs at 500 hPa; (b) the geopotential height (gpm; contour), equivalent potential temperature (K; shading), and superimposed with horizontal wind barbs at 850 hPa; (c) the geopotential height (gpm; contour), relative humidity (%; shading), and superimposed with horizontal wind barbs at 950 hPa; and (d) the surface pressure (Pa; contour), surface temperature (K; shading), and superimpose with surface wind barbs. The red line indicates the wind shear line at 850 hPa; the blue line with triangles depicts the cold front at surface. The Guangdong Province is indicated by blue curves.
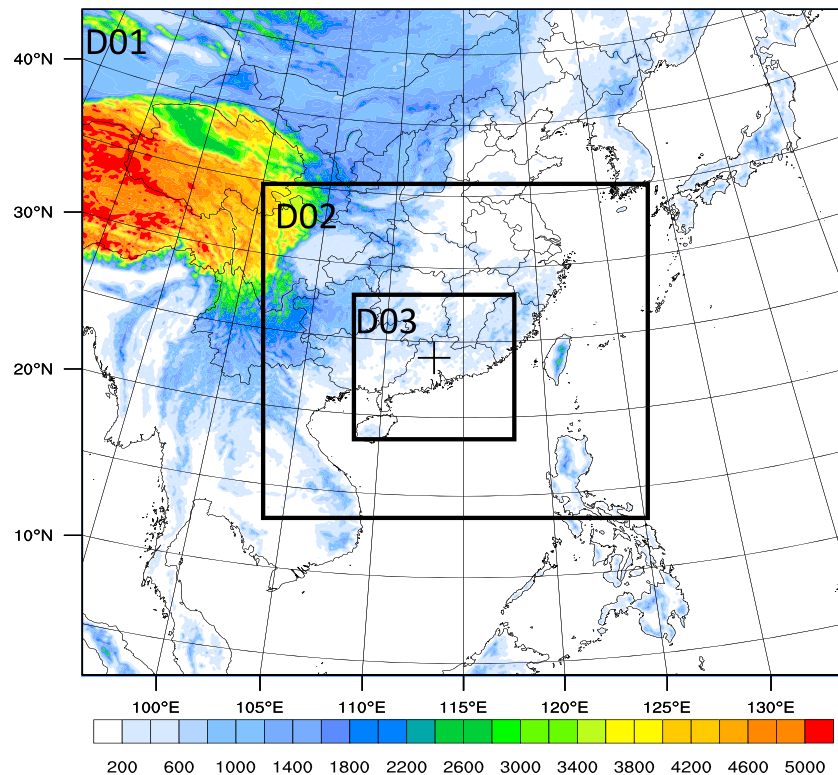


**Figure 5.** WRF model domain configuration (D01, D02, and D03) with terrain height (m; shading). The black cross indicates the location of Qingyuan.

**Table 1**
*Summary of WRF Experiments*

| Experiment | Latent Heating | Terrain | Purposes of Experiment |
|---|---|---|---|
| Control run | Yes | Real | Full physics control run |
| TER-A run | Yes | Increase surface 500 m over the land | The depth of stable layer (wave ducting) |
| TER-B run | Yes | Increase surface 500 m over the land and ocean | The depth of stable layer (wave ducting) |
| FakeDry-A run | No | Real | Latent heating effect (interactions of convection and waves) |
| FakeDry-B run | No latent heating from 1800 UTC | Real | Latent heating effect (interactions of convection and waves) |

lateral boundary conditions in the simulations. The Kain-Fritsch convection parameterization (Kain, 2004) is applied in the 9-km mesh outer domain but not applied in the inner domains (D02 and D03). The other physical parameterizations used include the Yonsei University boundary layer scheme (Hong et al., 2006), the Thompson microphysics scheme (Thompson et al., 2008), the Rapid Radiative Transfer Model for General Circulation Model long-wave and short-wave radiation scheme, the revised MM5 Monin-Obukhov surface-layer scheme (Jiménez et al., 2012), and the unified Noah land-surface-model scheme (Livneh et al., 2011).

Several sensitivity experiments are conducted (Table 1) to further examine and explore the relevant mechanisms proposed in the present study. The topography is raised by 500 m over the land in TER-A run, while the surface over the land and ocean are both elevated by 500 m in TER-B run. Owing to the changes of terrain heights in the TER-A and TER-B, the depth of the low-level stable layer is reduced accordingly. The two TER runs are analyzed to explain the effect of wave ducting as discussed in section 4.2. The objective of the two FakeDry runs is to reveal the role of convection on gravity waves and their interactions that will be discussed in section 4.3. In the FakeDry-A run, the latent heating is turned off from the beginning (1200 UTC), whereas in the FakeDry-B run the latent heating is turned off from 1800 UTC when the banded convection has already generated. The configurations of those sensitivity experiments are summarized in Table 1.

### 3.2. Evaluation of the Control Simulation

Comparing with the observation (Figure 1), the wavelike convective bands with respect to their spacing distance and propagation direction are captured reasonably well in the control run as shown in Figure 6, although the occurrence of the simulated wave pattern is delayed by a few hours and its location tends to be more to the south (ocean side). The exact reasons for such a bias are beyond the scope of this study, which may be due to the deficiency in the initial conditions used and/or imperfect model physics. Similar to the observation (Figure 1), the simulated convective bands orient northwest-to-southeast, move northeastward coherently, and persist for a long time (9 hr; Figure 6). The distance-time Hovömller diagrams of the observed and simulated radar reflectivity are further compared in Figure 3. The simulation also exhibits a significant wave pattern with a similar horizontal wavelength (~40–50 km) and wave speed (~12 m/s) as the observation (Figure 3). However, the simulated convective bands tend to be stronger, and their primary horizontal spacing distance (around ~40 km) is somewhat smaller than the observation (~50 km).

Next, the environments in the observations and simulations are compared using soundings (Figure 7). The observed and simulated vertical thermal profiles at 1200 UTC 30 January 2018 are quite similar (Figures 7b and 7c). In terms of moisture conditions, the atmosphere below 600 hPa is nearly saturated, but the layer above 600 hPa is quite dry. The low-level layer below 850 hPa is stable except for near the surface. The low-level stable layer is capped by a nearly neutral (moist stability) layer within 850–600 hPa. Besides the low-level stable layer, a stable layer exists aloft between 600 and 500 hPa. Such a vertical thermal pattern persists in the simulation until at least 1800 UTC 30 January (Figure 7d). The depths of the low-level stable layer
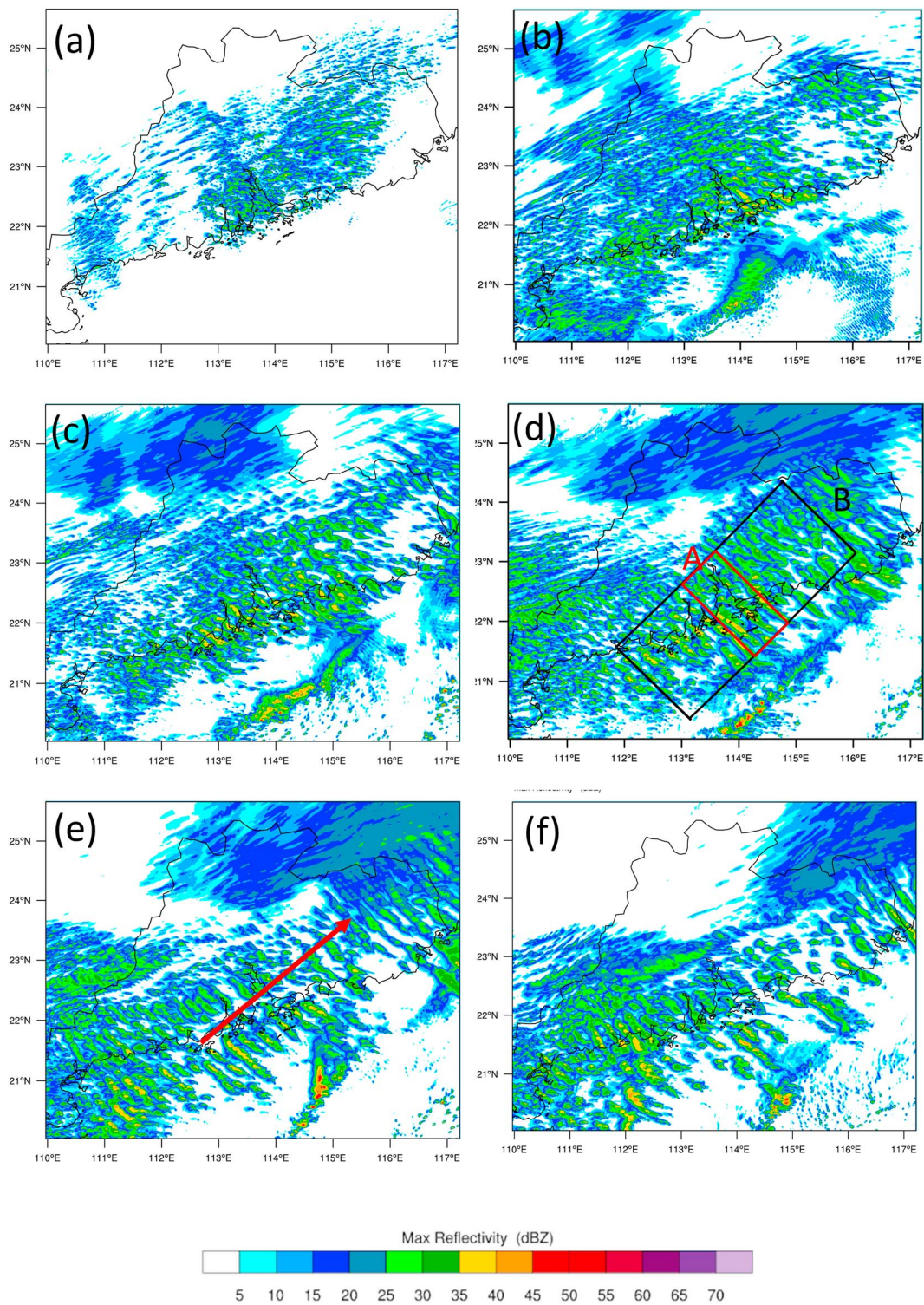
**Figure 6.** Simulated radar composite reflectivity on (a) 1300 UTC, (b) 1500 UTC, (c) 1700 UTC, (d) 1900 UTC, (e) 2100 UTC, and (f) 2300 UTC 30 January 2018 in the control run. The red arrow in Figure 6e indicates moving direction of convective bands. The red box A and black box B are shown in Figure 6d.
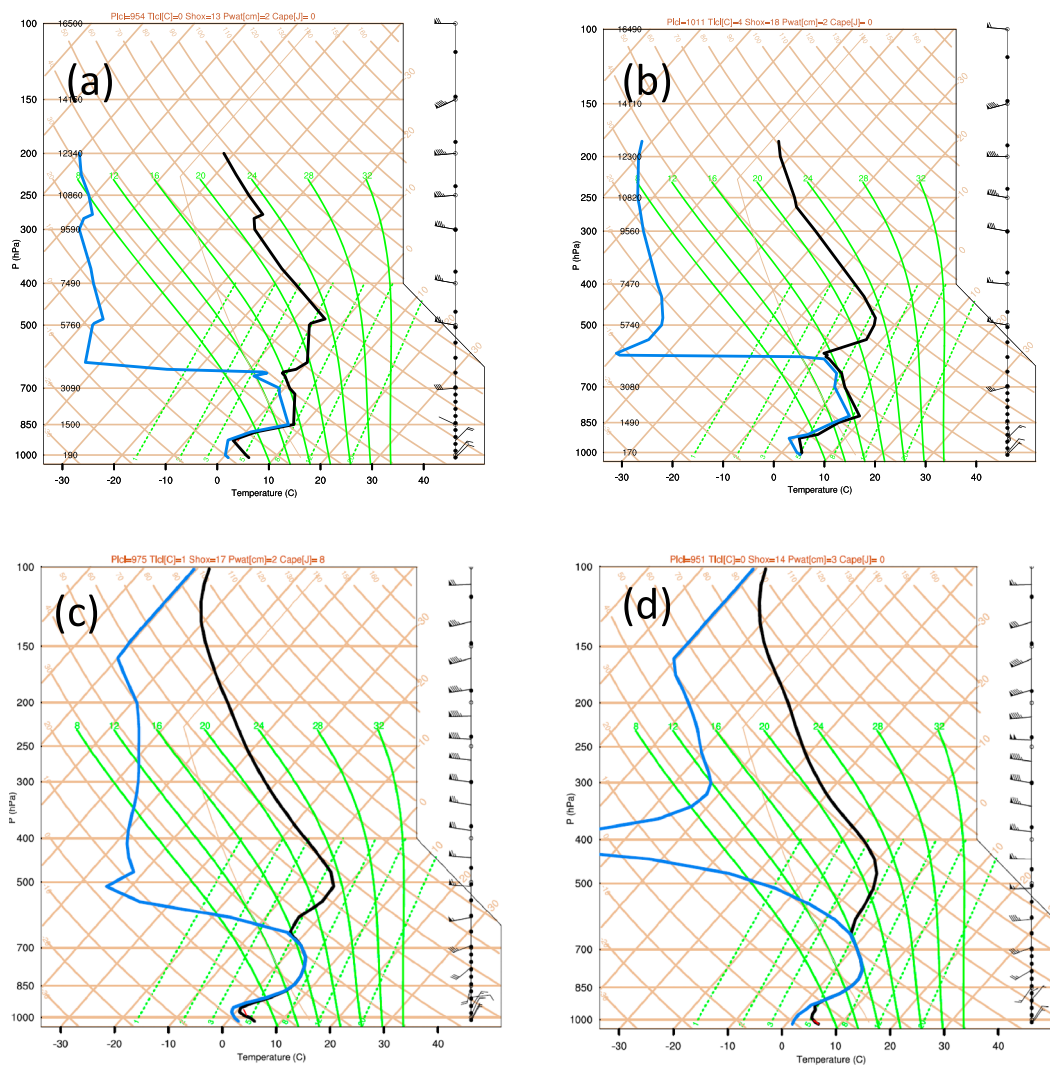
**Figure 7.** Skew T-log *p* diagrams at the Qingyuan at (a) 1200 UTC 29 January, (b) 1200 UTC 30 January from sounding observation, (c) 1200 UTC 30 January, and (d) 1800 UTC 30 January from the control run. The location of Qingyuan is indicated in Figure 5.

and the moist neutral layer are thinner at 1200 UTC 29 January 2018 (Figure 7a) when the banded convection does not occur (not shown), which is in contrast with that at 1200 UTC 30 January 2018 (Figure 7b) as the focus of the present study. In addition, strong low-level vertical wind shear occurs in the both observation and simulation (Figure 7).

## 4. Results

### 4.1. Banded Convection and Gravity Waves

To further illustrate the vertical structure of the convective bands and associated wave features, vertical cross sections of cloud water mixing ratio and vertical velocity along the direction of wave propagation and composited along the wavefront in red box A of Figure 6d are shown in Figure 8. There are three moderately deep convective bands extending to the 600-hPa level, whose spacing distance is around ~40 km. These moderately deep convective bands correspond to the strong upward motions with a maximum at around 700 hPa. Meanwhile, the vertical motion is relatively small or even downward between the convective bands. From their evolution (Figure 8), these convective bands move from the left to the
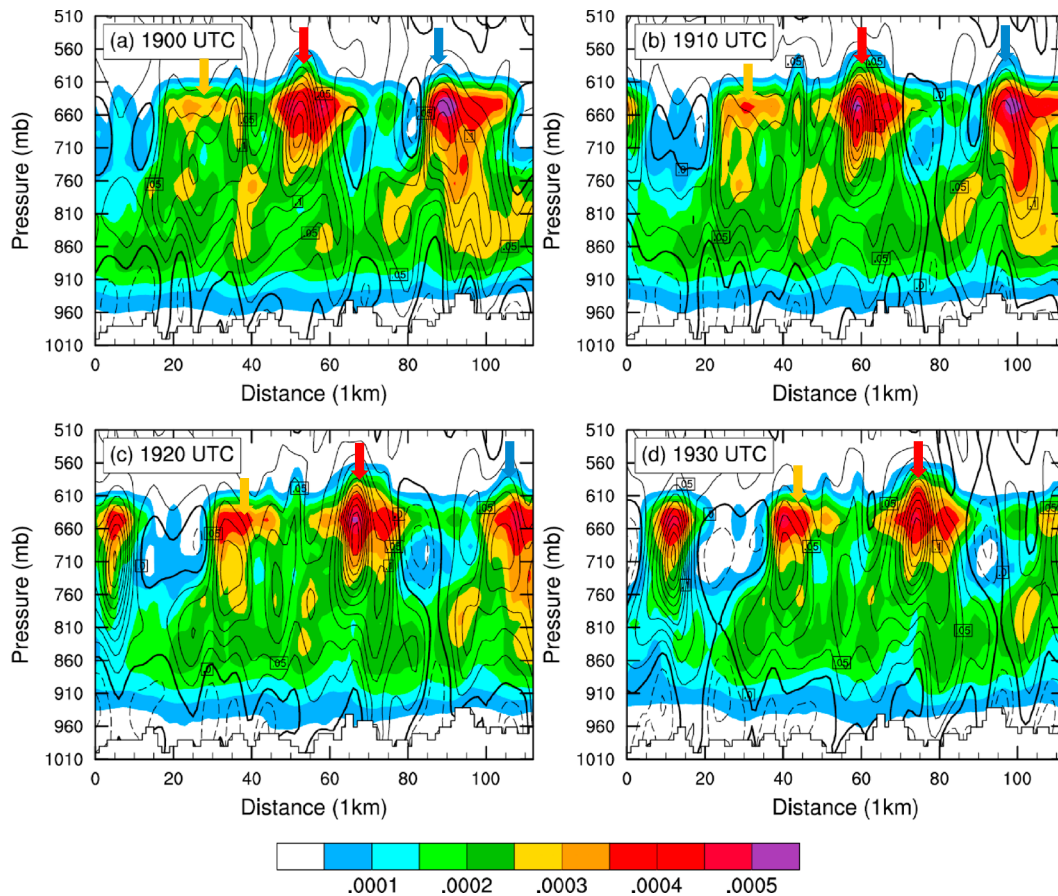
**Figure 8.** Wave-parallel vertical cross section of cloud water mixing ratio (shading; kg kg$^{-1}$) and vertical motion (m/s; contour) compositing (averaging) along the wavefronts in the red box A of Figure 6d at 1900, 1910, 1920, and 1930 UTC, 30 January 2018. The left (right) side of $x$ axis is southwest (northeast) side. The yellow, red, and blue arrows indicate the locations of individual moderately deep convective bands.

right (northeastward) accompanied by the maximum of upward motion. For instance, a convective cell indicated by a red arrow is located at the distance of 54 km at 1900 UTC, and it travels to the distance of 75 km at 1930 UTC. The propagation speed is thus calculated by 11.5 m/s. In addition, shallower convection featuring smaller spacing distance of around 15–20 km also exists between 900- and 750-hPa levels.

Two-dimensional (frequency-wave number) spectrum of the 4-km cloud mixing ratio is analyzed using a method similar to Wheeler and Kiladis (1999) as shown in Figure 9a in order to better quantify its temporal and spatial characteristics. Two overlapping 8-hr time intervals (0–8 and 4–12 hr) with 10-min time resolution are used for calculation. To highlight the spectrum peaks, the raw power spectrum is divided by the smoothed field following Wheeler and Kiladis (1999) and Lane and Zhang (2011). In Figure 9a, there are two notable sets of peaks in the frequency-wave number space. The primary peak occurs at the horizontal wavelength of ~40 km and at the period of ~50 min, whereas the secondary peak occurs at the horizontal wavelength of ~20 km and at the period of ~30 min. The line following the peaks indicates the phase speed of $\frac{\omega}{k} \approx 11.5$ m/s, which is roughly in agreement with the moving speed of the convective bands calculated previously in Figure 8. The primary peak represents the deeper convective bands with a larger wavelength and a longer period, while the secondary peak might be related to the shallower convection with a smaller wavelength and a shorter period. We also found two similar spectral peaks in the frequency-wave number space of the observed radar composite reflectivity (not shown). The observed primary peak occurs at the horizontal wavelength of ~50 km that is slightly larger than the simulated one (~40 km), while the secondary peaks in the observation and simulation are similar.
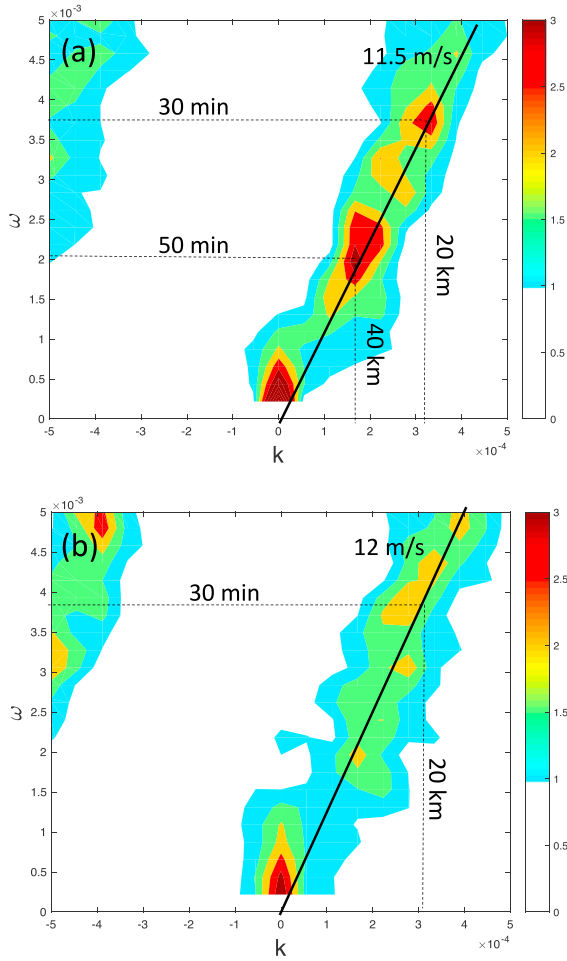
**Figure 9.** Power spectrum of the 4-km cloud mixing ratio in the red box A of Figure 6d divided by a smoothed background spectrum from (a) the control run and (b) the TER-B run. The black solid line depicts phase speed $\omega/k$. The black dashed lines indicate the horizontal wavelengths and wave periods for the peaks.

The horizontal distributions of surface pressure perturbation, vertical motion, and potential temperature at 900 hPa are shown in Figure 10 to illustrate the polarization relationship of those variables in the waves. The surface pressure perturbation is calculated by the deviation of current surface pressure (1900 UTC) and surface pressure at 1300 UTC. It clearly shows that the maximum of upward motion is located to the downstream (upstream) side of the largest surface pressure perturbation (potential temperature). Such fluctuations in the low troposphere (the polarization relation) correspond well to the basic gravity wave features (Eom, 1975). Based on the dispersion relation in the power spectrum diagram and the polarization relation described above, these waves are consistent with (and thus regarded here as) gravity waves that are coupled with convection.

### 4.2. Wave Ducting

Since the banded convective activity and the associated gravity waves persisted for nearly 10 hr, a wave duct might exist that could prohibit the energy of the gravity wave propagation upward and keep gravity waves propagating horizontally in the duct. In this section, we examine if the environment in this case could provide a wave duct of the simulated gravity waves.

Figure 11a shows a wave-parallel vertical cross section of equivalent potential temperature and winds at 1900 UTC when the banded convective activity is evident. The vertical gradient of the equivalent potential temperature is quite large at low levels (850–1,000 hPa) but fairly small at middle levels (850–500 hPa). The fluctuations in equivalent potential temperature at around 650 hPa are nearly in phase with those of cloud water mixing ratio. In addition, the wind in the wave propagation direction is negative at low levels and positive at middle levels, which indicates the strong wind shear at low levels.

The vertical distribution of moist static stability (or moist Brunt–Väisälä frequency $N_m$) is shown in Figures 11b and 12a. $N_m$ for the unsaturated air can be obtained as follows:

$$N_m^2 = \frac{d\ln\theta_v}{dz} \tag{4.1}$$

where $\theta_v = \theta \times (1 + 0.61q)$ is the virtual potential temperature and $q$ is the water vapor mixing ratio. Since the low-level atmosphere is saturated, the Brunt–Väisälä frequency should be replaced by a saturated version following Durran and Klemp (1982) as below:

$$N_m^2 = g\left\{ \frac{1 + (Lq_s/RT)}{1 + (\epsilon L^2 q_s/c_p RT^2)} \times \left( \frac{d\ln\theta}{dz} \frac{L}{c_p T} \frac{dq_s}{dz} \right) - \frac{dq_w}{dz} \right\} \tag{4.2}$$

where $T$ and $\theta$ are the sensible and potential temperatures of the atmosphere, $g$ is the gravitational acceleration, $q_s$ is the saturation mixing ratio, $q_w$ is the total water mixing ratio, $L$ is the latent heat of vaporization, $R$ is the ideal gas constant for dry air, $\epsilon = \frac{R}{R_v}$, $R_v$ is the gas constant for water vapor, and $c_p$ is the heat capacities of dry air.
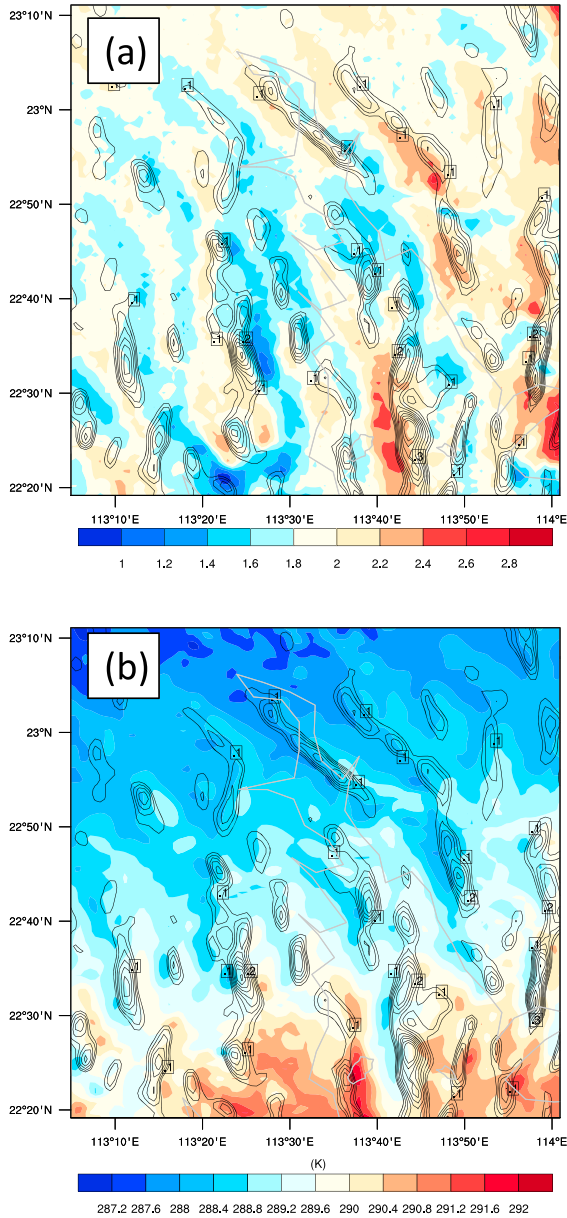
**Figure 10.** The horizontal distribution of vertical motion at 900 hPa (contour; >0.1 m/s with an interval of 0.05 m/s) and (a) perturbation surface pressure (hPa; shading) and (b) potential temperature at 900 hPa (K; shading) at 1900 UTC 30 January 2018 from the control run. The area is near the box A of Figure 6d.

As shown in Figures 11b and 12a, $N_m$ is large (>0.012 s$^{-1}$) below 850 hPa (or ~1,500 m) with a maximum of 0.02 s$^{-1}$ at 950 hPa. $N_m$ within 850–650 hPa is relatively small and nearly close to 0, and $N_m$ above 650 hPa becomes large again. Thus, three layers exist with different static stability: the low-level stable layer is capped by the middle-level less stable layer, whereas the less stable layer is also overlaid by an aloft stable layer. According to Lindzen and Tung (1976), the environment is conducive for a typical wave duct setting, but other critical factors need to be further examined, such as the existence of a steering level and the small values of the Richardson number.

The steering level, which refers to a level where the ground-relative phase speed of wave (11.5 m/s in Figure 9a) equals to the background wind speed in the wave propagation direction ($\overline{U}$), is at around 750-hPa level (2,500 m; Figures 11b and 12b) in the present case. Figure 11b shows the local gradient Richardson number

$$\mathrm{Ri} = \frac{N_m^2}{\left(\frac{\partial \overline{U}}{\partial z}\right)^2} \tag{4.3}$$

less than 1/4 occurs within the 850–700-hPa layer. The small-Ri layer and the critical level are both embedded in the middle-level less stable layer. Therefore, the less stable sheared layer, with Ri < 1/4 and a critical level imbedded, is an overreflection region of gravity waves based on the wave ducting model in Lindzen and Tung (1976).

The intrinsic ducted wave speed is given as

$$C_{d,n} = \frac{N_m D}{\left(\frac{\pi}{2} + n\right)} \tag{4.4}$$

where $n$ indicates different vertical wave modes and $D$ is the depth of the low-level stable layer. In the primary mode ($n = 0$), the intrinsic wave phase speed is calculated to be 15.2 m/s, given $D$ is 1.5 km (a stable layer with moist static stability greater than 0.012 s$^{-1}$) and the averaged $N_m$ in the stable layer is 0.016 s$^{-1}$ (Figure 12a). Considering the mean background wind in the wave-parallel direction in the stable layer is ~−3 m/s (Figure 12b), the calculated ground-relative wave phase speed is 12.2 m/s, which is in close agreement with the simulated ground-relative wave phase speed of around 11.5 m/s (Figure 9a).

The vertical wavelength of the gravity wave $\lambda_z$ that is related to the stable-layer depth as follow

$$\lambda_z = 4 \times D \tag{4.5}$$

is 6 km (Lindzen & Tung, 1976; Zhang et al., 2001; Zhang & Koch, 2000). The dispersion relationship of a two-dimensional gravity wave with a background wind is

$$\left(\omega - k\overline{U}\right)^2 = \frac{N_m^2 k^2}{k^2 + m^2} \tag{4.6}$$

where $m$ and $k$ are the vertical and horizontal wave numbers. When $k \ll m$, the dispersion relationship can be further expressed as
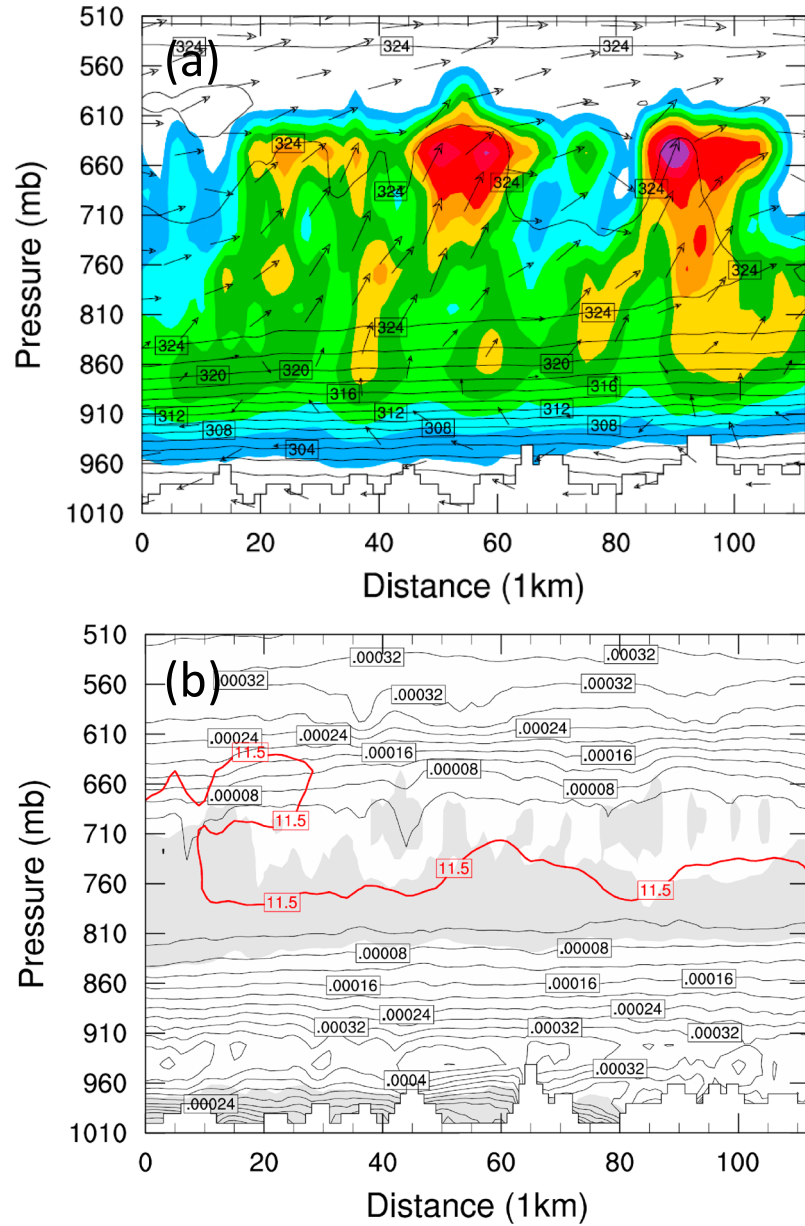
**Figure 11.** (a) Wave-parallel vertical cross section of cloud water mixing ratio (shading; kg kg$^{-1}$), equivalent potential temperature (K; contour), and flow vectors (black vectors; wind component along the cross section and 100 times vertical velocity) compositing along the wavefronts in the red box A of Figure 6d at 1900 UTC 30 January 2018. (b) Same as in (a) expect for square of moist Brunt–Väisälä frequency (s$^{-2}$; contour). The gray shading indicates Richardson number Ri <0.25 and the red line shows the critical level, assuming a wave speed of 11.5 m/s.

$$\lambda_x = T\left(\frac{N_m \lambda_z}{2\pi} + \overline{U}\right) \tag{4.7}$$

where $\lambda_x = 2\pi/k$ is the horizontal wavelength, $\lambda_z = 2\pi/m$ is the vertical wavelength, and $T = 2\pi/\omega$ is the wave period. Given the primary and secondary wave periods are 50 and 30 min (Figure 9a), the calculated primary and secondary $\lambda_x$ are 36.6 and 22 km, which also compare well with the simulated horizontal wavelengths of 40 and 20 km, respectively. The primary and secondary wave periods might be
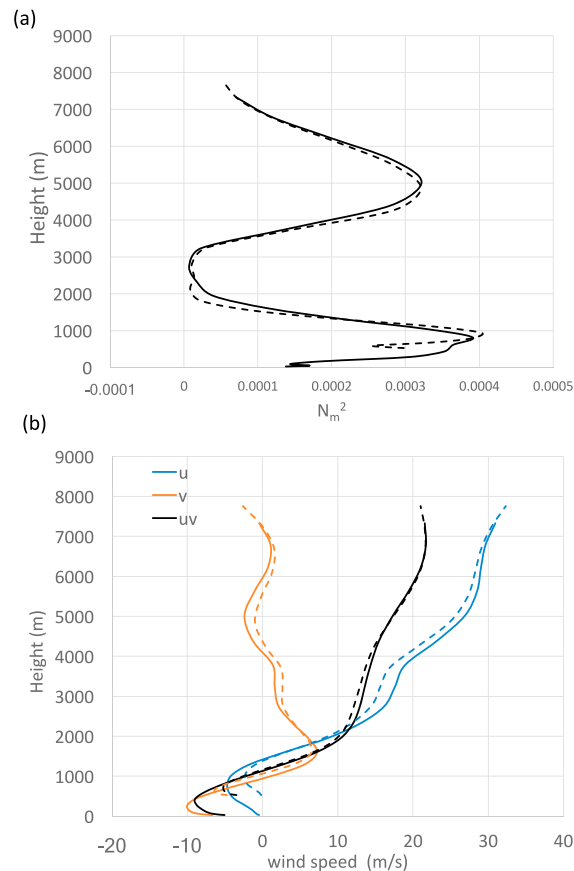
**Figure 12.** Vertical profiles of (a) square of moist Brunt–Väisälä frequency and (b) zonal wind ($u$), meridional wind ($v$), and wind speed in southwesterly direction ($uv$) averaged in red region A of Figure 6d from the control run (solid lines) and the TER-B run (dashed lines).

related to the life cycles of moderately deep convection and shallower convection, respectively, which will be discussed in the next subsection.

Two sensitivity experiments (TER-A and TER-B) with respect to the change of the stable layer depth are designed and conducted to further examine the important role of wave ducting in the generation and maintenance of the gravity waves. With raised terrain heights in the sensitivity experiments, the depth of the stable layer decreases to 1 km (500–1,500 m; Figure 12a) and the layer with the negative background wind in the wave propagation direction becomes shallow (Figure 12b). In the TER-A that the terrain over the land is raised by 500 m, the wave pattern over the land becomes weaker with a smaller horizontal wavelength, but it remains evident over the ocean with a larger horizontal wavelength (Figures 13a, 14a, and 14b). In the TER-B that the surface elevations of the ocean and land are both raised by 500 m, the wave features over the land and ocean are both not as evident with a smaller horizontal wavelength than the control run. Furthermore, we examine the wave duct theory in the TER-B run using equation (4.4). Given $D$ is 1 km and the averaged $N_m$ in the stable layer is 0.018 s$^{-1}$ (Figure 12a), the calculated intrinsic wave speed is 11.5 m/s for the primary mode ($n = 0$). Therefore, the calculated ground-relative wave speed is 11.5 m/s under mean background wind of 0 m/s (Figure 12b), which is also roughly consistent with the simulated ground-relative wave speed of 12 m/s (Figure 9b). In addition, a thinner stable layer determines a shorter vertical and horizontal wavelength of gravity waves according to equations (4.5) and (4.7), which might thus affect the depth and horizontal spacing of convection. As shown in Figures 14b and 14c, the vertical scale (800–650 hPa) and horizontal spacing (10–20 km) of convection in the TER-A and TER-B runs are indeed
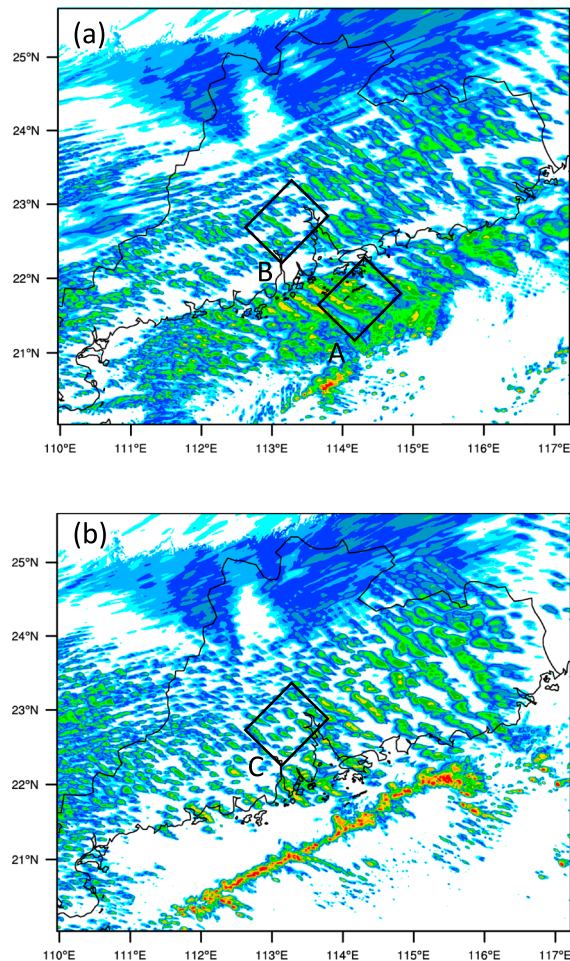
**Figure 13.** Simulated radar composite reflectivity at 1900 UTC 30 January 2018 from (a) the TER-A run and (b) the TER-B run. The black regions A, B, and C shown are used in Figure 14.

smaller than those in the control run (900–600 hPa) as expected by the wave duct theory. The power spectrum in the TER-B (Figure 9b) indicates the primary horizontal wavelength of ~20 km and wave period of ~30 min, which is different from the control run.

Therefore, in the present study, wave-ducting mechanism serves as an important mechanism of maintenance and also selects the wave modes. The next subsection will focus on how gravity waves interact with convection.

### 4.3. The Interactions of Convection and Waves

A popular theory explaining the interactions of convection and gravity waves is the wave-CISK hypothesis in which gravity wave can trigger and modulate convection, whereas convection maintains and amplifies the waves through a positive feedback process with latent heating. It is noted that the wave-CISK hypothesis has not been strictly proven, but some signatures and evidences can be examined to indicate the wave-convection interactions.

In the present study, the banded convective lines traveling synergistically with the waves (the maximum of upward motion; Figure 8) suggest the coupling of gravity waves and convection (Powers, 1997; Powers & Reed, 1993; Zhang et al., 2001). The strongest upward motion is concentrated around the critical level
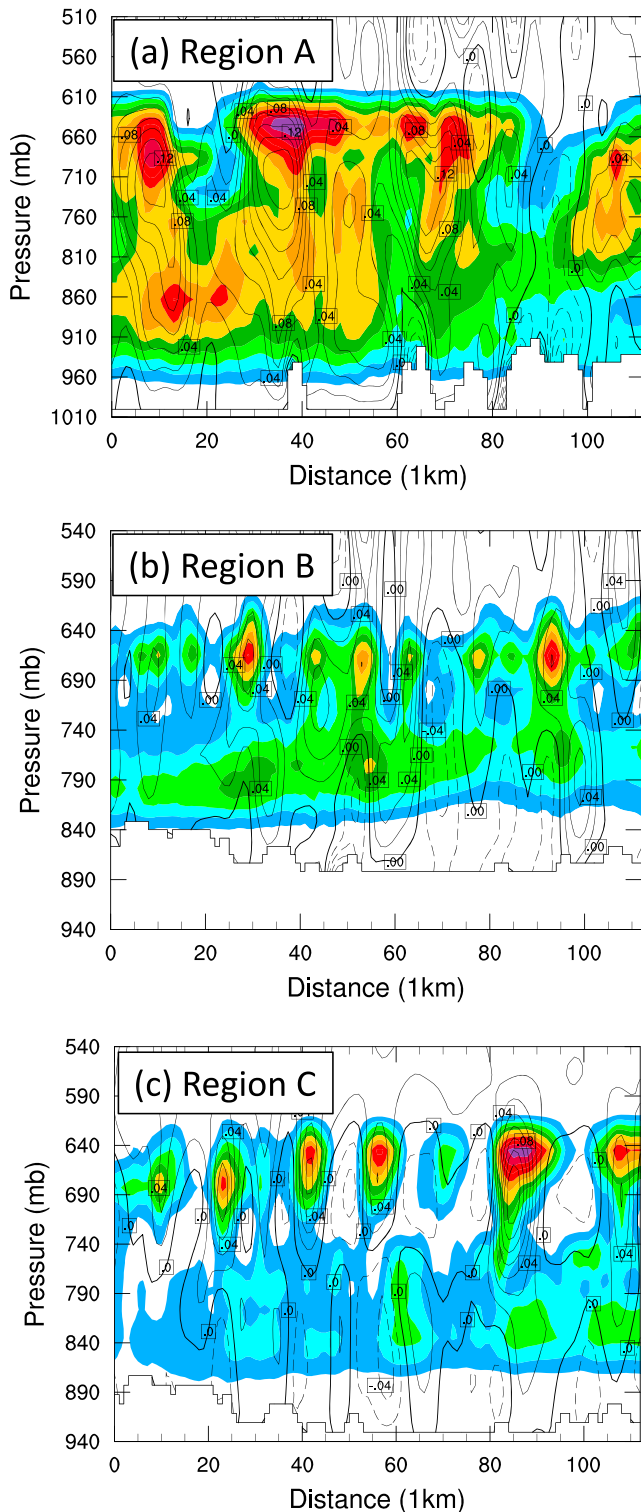
**Figure 14.** Wave-parallel vertical cross section of cloud water mixing ratio (shading; kg kg$^{-1}$) and vertical motion (m/s; contour) compositing along the wavefronts in the black boxes (a) A, (b) B, and (c) C of Figure 13 at 1900 UTC, 30 January 2018 from (a and b) the TER-A and (c) the TER-B run.

(Figures 8a and 11b), which differs from the pure linear ducting theory suggesting that wave-convection interactions might indeed play a key role in the present study.

In order to study the impact of latent heat in the convection on gravity waves in this case, two sensitivity experiments on latent heating (FakeDry-A and FakeDry-B) are conducted. If the latent heat is turned off at the beginning (1200 UTC, FakeDry-A), the simulated radar reflectivity of convection is not as large as in the control run (Figures 15a and 15b). Especially, the wave pattern of convection almost disappeared in the FakeDry-A run. From the vertical structure of moisture and vertical motion in the FakeDry-A run (Figure 16a), two layers of high water vapor mixing ratio occur at the 850- and 700-hPa levels, respectively. In the absence of latent heating, the condensation of water vapor is much smaller compared to the control run. Without the energy released from convective instability through condensational heating, convection cannot develop properly. Meanwhile, the wave pattern of the vertical motion at middle levels changes and becomes much weaker than that in the control run (Figure 16a).

Furthermore, in the FakeDry-B run, that the latent heat is turned off at 1800 UTC when the wavelike convection has been already generated (Figure 15c), the banded precipitation lines still persist (Figure 15d) but the wave features are not as evident as before (Figure 15c) while the horizontal wavelength becomes smaller (Figure 15d). As shown in the vertical cross section of the FakeDry-B run (Figure 16b), the shallower convection at around 850 hPa still retains some wave characteristics at 1900 UTC with a smaller horizontal wavelength (Figure 16b). In the absence of latent heat after 1800 UTC, the development of moderately deep convection cannot be supported any more (Figure 16b). The strongest upward motion occurs lower (around 800–700 hPa) than that in the control run, while the high cloud water mixing ratio is constrained below 600 hPa. Nevertheless, shallower clouds can still be generated under the effect of ducted gravity waves that has initiated before 1800 UTC which persist in the duct in an hour. Since the life cycle of shallow precipitation is shorter than that of moderately deep convection, the shorter wave period (30 min) may be selected as the primary mode; the smaller horizontal wavelength (20 km) is seen to be dominant in the FakeDry-B run based on equation (4.7). Therefore, the primary and secondary wave periods might be related to the life cycles of moderately deep convection and shallower convection, respectively. But how the life cycles of convection affect the wave periods and thus determine the horizontal wavelengths needs to be further investigated in the future.

Therefore, the two sensitivity experiments indicate a positive feedback process and interactions of convection and gravity waves through the latent heating. The latent heating from moist convection is an important energy source of the gravity waves that amplifies the waves, which is regarded as a wave-CISK mode (Koch et al., 1988; Powers, 1997; Zhang et al., 2001). Although some signatures and evidence of the wave-convection interaction are presented in the current study, a more thorough and theoretical exploration of wave-convection interaction (wave-CISK) needs to be further investigated but is beyond the scope of the current study.
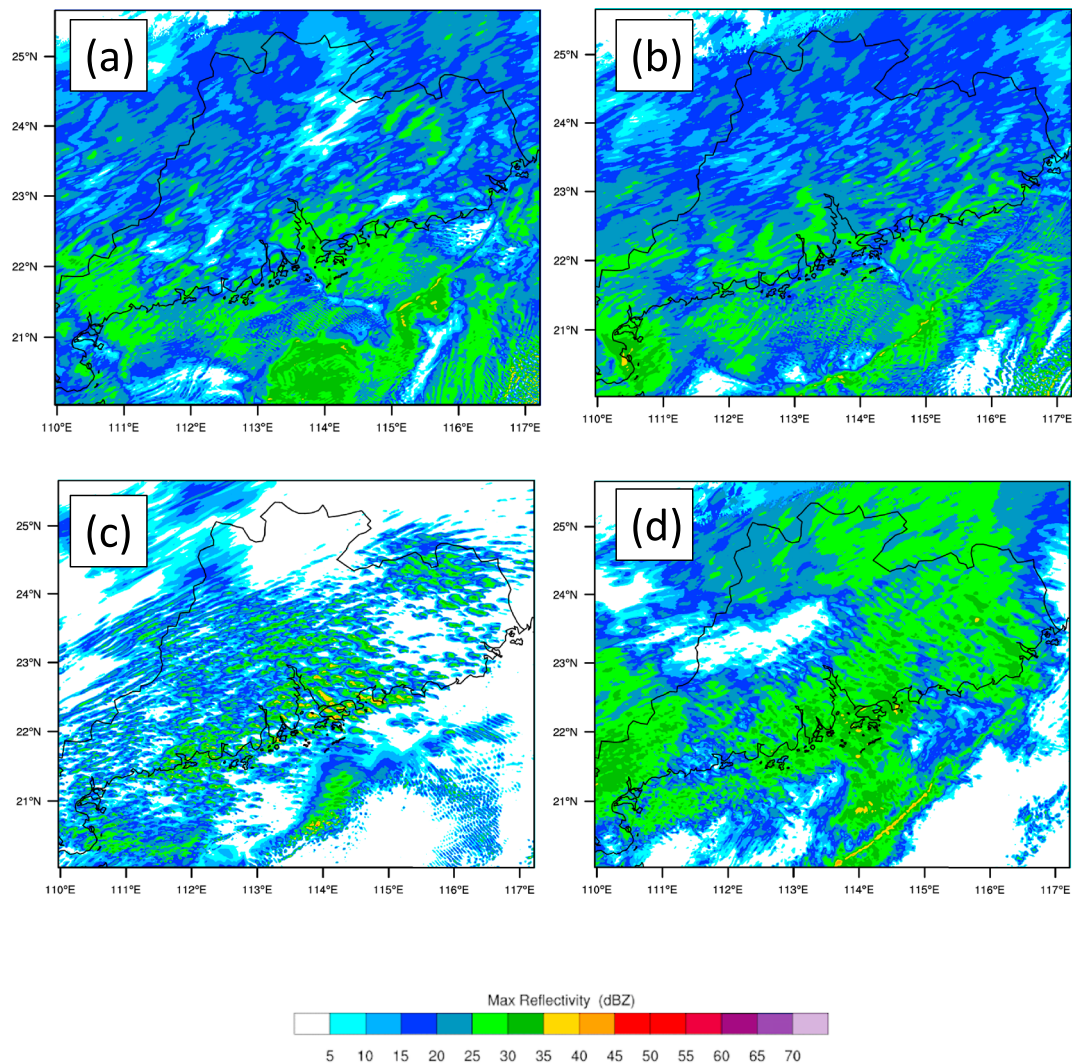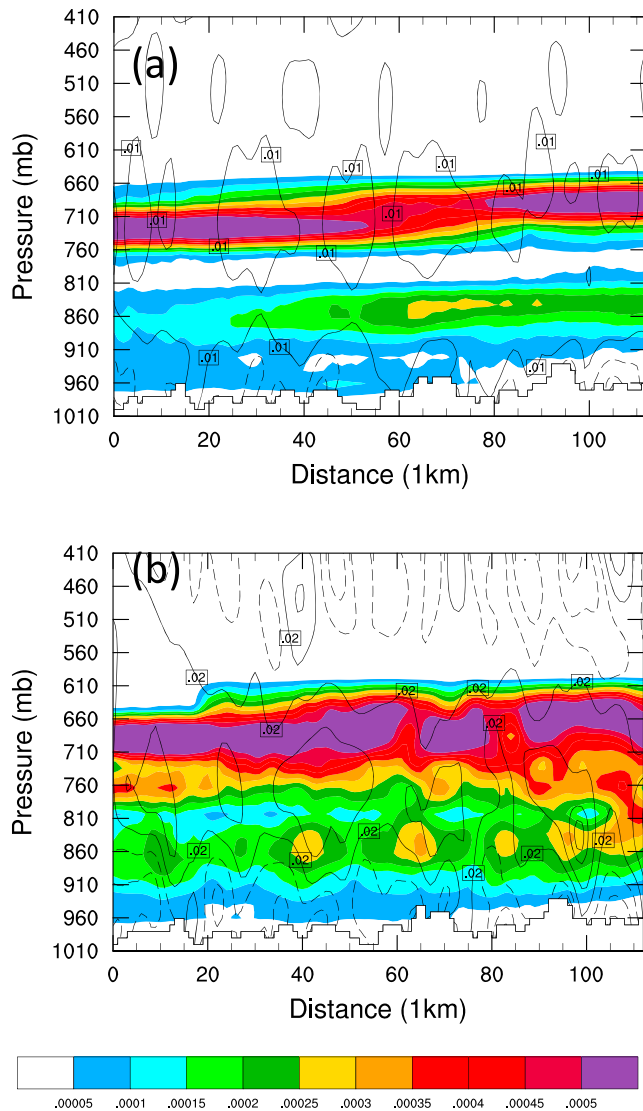
**Figure 15.** Simulated radar composite reflectivity on (a and c) 1700 UTC and (b and d) 1900 UTC 30 January 2018 from (a and b) the FakeDry-A run and (c and d) the FakeDry-B run.

## 5. Summary

In the present study, we use the Advanced Research Weather Research and Forecasting model with 1-km horizontal grid spacing to investigate the characteristics and mechanisms of an episode of banded convective activity associated with gravity waves near the south coast of China that occurred on 30 January 2018. Several northwest-southeast oriented convective bands were generated and maintained for nearly 10 hr over Guangdong Province in South China. They propagated northeastward at a speed of around 12 m/s with their main horizontal spacing distance of ~50 km and exhibited apparent wave characteristics. The convection-allowing simulations can capture reasonably well the wavelike banded convection with a broadly similar horizontal wavelength (~40 km) and also associated atmospheric conditions, although the banding appears later and stronger than in the observations. The major findings are summarized as below.

1. Hovmöller diagrams and power spectrum analysis indicate that simulated gravity waves in the banded convective activity feature a similar wave phase speed of around 11.5 m/s compared to the observation. Two main simulated wavelengths exist, which are 40 km (primary) and 20 km (secondary) with the corresponding wave periods of 50 and 30 min, respectively.

**Figure 16.** Same as in Figure 8a expect for (a) the FakeDry-A run and (b) the FakeDry-B run.

2. In this case, a strong stable layer below 850 hPa is capped by a moist neutral stability layer within 850–600 hPa. Strong vertical shear occurs at low levels, and the northeasterly (southwesterly) winds prevail at low (middle) levels. A critical level, where the mean background wind in the southwest-northeast direction is equal to the wave phase speed (11.5 m/s), is embedded in the moist neutral stability layer. A shallow layer with Richardson number less than 1/4 surrounds the critical level. Such an environment supports a wave duct of gravity waves to maintain the energy in the duct based on the theory of Lindzen and Tung (1976).

3. In the theory of wave ducting, the intrinsic wave speed is closely related to the strength and depth of the low-level stable layer ($C_d = \frac{N_m D}{\left(\frac{\pi}{2}+n\right)}$). The calculated ground-relative wave speed (12.2 m/s) is well in agreement with the simulated one (11.5 m/s). The horizontal wavelength might be associated with the life cycle of convection in addition to the stable layer. In the sensitivity experiment that the depth of stable layer is reduced, the wave speed and wavelength are still in line with the wave duct theory.

4. The strongest upward motion that is concentrated around the critical level traveled with convection synergistically, suggesting the interactions of convection and gravity waves. The wave features almost disappear when the latent heating is turned off in the sensitivity simulation. The latent heating from moist convection may amplify the ducted gravity waves and play a key role in the formation and maintenance of gravity waves.

It is found that wave ducting and wave-convection interaction (or called "wave-CISK hypothesis") co-existed in the present case. This ducted wave-CISK mode has been recognized by Powers and Reed (1993), and Zhang et al. (2001). The wave ducting mechanism is responsible for selecting the horizontal scale and speed of the wave modes that can be maintained and supported by the wave duct. The selected gravity waves can trigger and modulate convection, which in turn can maintain and strengthen the gravity waves through a positive feedback process that is consistent with the wave-CISK hypothesis (which to a certain degree is not strictly proven). The detailed interactions of two mechanisms and their relative importance is a very interesting issue that needs to be further addressed in the future. In addition, we found that the simulations of banded convection and associated gravity waves are highly sensitive to the initial conditions and spatial resolution (not shown). The ability to predict nonlinear phenomena such as studied here is challenging (e.g., Sun & Zhang, 2016; Zhang et al., 2007), so further study is important for forecasting applications.

## References

Adams-Selin, R. D., & Johnson, R. H. (2013). Examination of gravity waves associated with the 13 March 2003 bow echo. *Monthly Weather Review*, *141*(11), 3735–3756. https://doi.org/10.1175/MWR-D-12-00343.1

Alexander, M. J., Holton, J. R., & Durran, D. R. (1995). The gravity wave response above deep convection in a squall line simulation. *Journal of the Atmospheric Sciences*, *52*(12), 2212–2226. https://doi.org/10.1175/1520-0469(1995)052<2212:TGWRAD>2.0.CO;2

Booker, J., & Bretherton, F. (1967). The critical layer for internal gravity waves in a shear flow. *Journal of Fluid Mechanics*, *27*(03), 513–539. https://doi.org/10.1017/S0022112067000515

Bosart, L., Bracken, W., & Seimon, A. (1998). A study of cyclone mesoscale structure with emphasis on a large-amplitude inertia-gravity wave. *Monthly Weather Review*, *126*(6), 1497–1527. https://doi.org/10.1175/1520-0493(1998)126<1497:ASOCMS>2.0.CO;2

Bosart, L. F., & Cussen, J. P. (1973). Gravity wave phenomena accompanying east coast cyclogenesis. *Monthly Weather Review*, *101*(5), 446–454. https://doi.org/10.1175/1520-0493(1973)101<0446:GWPAEC>2.3.CO;2

Cram, J. M., Pielke, R. A., & Cotton, W. R. (1992). Numerical simulation and analysis of a prefrontal squall line. Part II: Propagation of the squall line as an internal gravity wave. *Journal of the Atmospheric Sciences*, *49*(3), 209–225. https://doi.org/10.1175/1520-0469(1992)049<0209:NSAAOA>2.0.CO;2

Crook, N. A. (1988). Trapping of low-level internal gravity waves. *Journal of the Atmospheric Sciences*, *45*(10), 1533–1541. https://doi.org/10.1175/1520-0469(1988)045<1533:TOLLIG>2.0.CO;2

Du, Y., & Chen, G. X. (2019). Heavy rainfall associated with double low-level jets over southern China. Part II: Convection initiation. *Monthly Weather Review*, *147*(2), 543–565. https://doi.org/10.1175/MWR-D-18-0102.1

Einaudi, F., & Lalas, D. P. (1973). On the growth rate of an unstable disturbance in a gravitationally stratified shear flow. *Journal of the Atmospheric Sciences*, *30*(8), 1707–1710. https://doi.org/10.1175/1520-0469(1973)030<1707:OTGROA>2.0.CO;2

Eom, J. K. (1975). Analysis of the internal gravity wave occurrence of 19 April 1970 in the Midwest. *Monthly Weather Review*, *103*(3), 217–226. https://doi.org/10.1175/1520-0493(1975)103<0217:AOTIGW>2.0.CO;2

Fovell, R. G., Mullendore, G. L., & Kim, S. (2006). Discrete propagation in numerically simulated nocturnal squall lines. *Monthly Weather Review*, *134*(12), 3735–3752. https://doi.org/10.1175/MWR3268.1

Fritts, D. C., & Alexander, M. J. (2003). Gravity wave dynamics and effects in the middle atmosphere. *Reviews of Geophysics*, *41*(1), 1003. https://doi.org/10.1029/2001RG000106

Hong, S., Noh, Y., & Dudhia, J. (2006). A new vertical diffusion package with an explicit treatment of entrainment processes. *Monthly Weather Review*, *134*(9), 2318–2341. https://doi.org/10.1175/MWR3199.1

Jiménez, P. A., Dudhia, J., González-Rouco, J. F., Navarro, J., Montávez, J. P., & García-Bustamante, E. (2012). A revised scheme for the WRF surface layer formulation. *Monthly Weather Review*, *140*(3), 898–918. https://doi.org/10.1175/MWR-D-11-00056.1

Jones, W. (1968). Reflexion and stability of waves in stably stratified fluids with shear flow: A numerical study. *Journal of Fluid Mechanics*, *34*(03), 609–624. https://doi.org/10.1017/S0022112068002119

Kain, J. S. (2004). The Kain–Fritsch convective parameterization: An update. *Journal of Applied Meteorology and Climatology*, *43*(1), 170–181. https://doi.org/10.1175/1520-0450(2004)043<0170:TKCPAU>2.0.CO;2

Koch, S. E., Golus, R. E., & Dorian, P. B. (1988). A mesoscale gravity wave event observed during CCOPE. Part II: Interactions between mesoscale convective systems and the antecedent waves. *Monthly Weather Review*, *116*(12), 2545–2569. https://doi.org/10.1175/1520-0493(1988)116<2545:AMGWEO>2.0.CO;2

Koch, S. E., Zhang, F., Kaplan, M. L., Lin, Y.-L., Weglarz, R., & Trexler, C. M. (2001). Numerical simulation of a gravity wave event observed during CCOPE. Part III: Mountain–plain solenoids in the generation of the second wave episode. *Monthly Weather Review*, *129*(5), 909–933. https://doi.org/10.1175/1520-0493(2001)129<0909:NSOAGW>2.0.CO;2

Kruse, C. G., & Smith, R. B. (2015). Gravity wave diagnostics and characteristics in mesoscale fields. *Journal of the Atmospheric Sciences*, *72*(11), 4372–4392. https://doi.org/10.1175/JAS-D-15-0079.1

Kusunoki, K., Eito, H., & Akaeda, K. (2000). A case study of low-level internal gravity waves using Doppler radar and ACARS. *Journal of the Meteorological Society of Japan. Ser. II*, *78*(5), 511–525. https://doi.org/10.2151/jmsj1965.78.5_511

Lac, C., Lafore, J.-P., & Redelsperger, J.-L. (2002). Role of gravity waves in triggering deep convection during TOGA-COARE. *Journal of the Atmospheric Sciences*, *59*(8), 1293–1316. https://doi.org/10.1175/1520-0469(2002)059<1293:ROGWIT>2.0.CO;2

Lane, T. P. (2015). Gravity waves|convectively generated gravity waves. *Encyclopedia of Atmospheric Sciences.*, 171–179.

Lane, T. P., & Reeder, M. J. (2001). Convectively generated gravity waves and their effect on the cloud environment. *Journal of the Atmospheric Sciences*, *58*(16), 2427–2440. https://doi.org/10.1175/1520-0469(2001)058<2427:CGGWAT>2.0.CO;2

Lane, T. P., & Zhang, F. (2011). Coupling between gravity waves and tropical convection at mesoscales. *Journal of the Atmospheric Sciences*, *68*(11), 2582–2598. https://doi.org/10.1175/2011JAS3577.1

Li, L., & Chen, Y. (2017). Numerical simulations of two trapped mountain lee waves downstream of Oahu. *Journal of Applied Meteorology and Climatology*, *56*(5), 1305–1324. https://doi.org/10.1175/JAMC-D-15-0341.1

Lin, Y.-L., & Goff, R. C. (1988). A study of a mesoscale solitary wave in the atmosphere originating near a region of deep convection. *Journal of the Atmospheric Sciences*, *45*(2), 194–206. https://doi.org/10.1175/1520-0469(1988)045<0194:ASOAMS>2.0.CO;2

Lindzen, R. S. (1974). Wave-CISK in the tropics. *Journal of the Atmospheric Sciences*, *31*(1), 156–179. https://doi.org/10.1175/1520-0469(1974)031<0156:WCITT>2.0.CO;2

Lindzen, R. S., & Tung, K.-K. (1976). Banded convective activity and ducted gravity waves. *Monthly Weather Review*, *104*(12), 1602–1617. https://doi.org/10.1175/1520-0493(1976)104<1602:BCAADG>2.0.CO;2

Liu, C., & Moncrieff, M. W. (2004). Effects of convectively generated gravity waves and rotation on the organization of convection. *Journal of the Atmospheric Sciences*, *61*(17), 2218–2227. https://doi.org/10.1175/1520-0469(2004)061<2218:EOCGGW>2.0.CO;2

Liu, L., Ran, L. K., & Gao, S. T. (2018). Analysis of the characteristics of inertia-gravity waves during an orographic precipitation event. *Advances in Atmospheric Sciences*, *35*(5), 604–620. https://doi.org/10.1007/s00376-017-7159-2

Livneh, B., Restrepo, P. J., & Lettenmaier, D. P. (2011). Development of a unified land model for prediction of surface hydrology and land–atmosphere interactions. *Journal of Hydrometeorology*, *12*(6), 1299–1320. https://doi.org/10.1175/2011JHM1361.1

Miller, D. A., & Sanders, F. (1980). Mesoscale conditions for the severe convection of 3 April 1974 in the east-Central United States. *Journal of the Atmospheric Sciences*, *37*(5), 1041–1055. https://doi.org/10.1175/1520-0469(1980)037<1041:MCFTSC>2.0.CO;2

Nappo, C. J. (2002). *An Introduction to Atmospheric Gravity Waves* (p. 276). San Diego: Academic Press.

Plougonven, R., & Zhang, F. (2015). Gravity waves|Gravity waves excited by jets and fronts. *Encyclopedia of Atmospheric Sciences*, 164–170. https://doi.org/10.1016/B978-0-12-382225-3.00498-9

Powers, J. G. (1997). Numerical model simulations of a mesoscale gravity wave event: Sensitivity tests and spectral analyses. *Monthly Weather Review*, *125*(8), 1838–1869. https://doi.org/10.1175/1520-0493(1997)125<1838:NMSOAM>2.0.CO;2

Powers, J. G., & Reed, R. J. (1993). Numerical simulation of the large-amplitude mesoscale gravity-wave event of 15 December 1987 in the Central United States. *Monthly Weather Review*, *121*(8), 2285–2308. https://doi.org/10.1175/1520-0493(1993)121<2285:NSOTLA>2.0.CO;2

Ralph, F. M., Crochet, M., & Venkateswaran, S. V. (1993). Observations of a mesoscale ducted gravity wave. *Journal of the Atmospheric Sciences*, *50*(19), 3277–3291. https://doi.org/10.1175/1520-0469(1993)050<3277:OOAMDG>2.0.CO;2

Raymond, D. J. (1975). A model for predicting the movement of continuously propagating convective stroms. *Journal of the Atmospheric Sciences*, *32*(7), 1308–1317. https://doi.org/10.1175/1520-0469(1975)032<1308:AMFPTM>2.0.CO;2

Raymond, D. J. (1987). A forced gravity wave model of self-organizing convection. *Journal of the Atmospheric Sciences*, *44*(23), 3528–3543. https://doi.org/10.1175/1520-0469(1987)044<3528:AFGWMO>2.0.CO;2

Rosenthal, A. J., & Lindzen, R. S. (1983). Instabilities in a stratified fluid having one critical level. Part II: Explanation of gravity wave instabilities using the concept of overreflection. *Journal of the Atmospheric Sciences*, *40*(3), 521–529. https://doi.org/10.1175/1520-0469(1983)040<0521:IIASFH>2.0.CO;2

Ruppert, J. H., & Bosart, L. F. (2014). A case study of the interaction of a mesoscale gravity wave with a mesoscale convective system. *Monthly Weather Review*, *142*(4), 1403–1429. https://doi.org/10.1175/MWR-D-13-00274.1

Schmidt, J. M., & Cotton, W. R. (1990). Interactions between upper and lower tropospheric gravity waves on squall line structure and maintenance. *Journal of the Atmospheric Sciences*, *47*(10), 1205–1222. https://doi.org/10.1175/1520-0469(1990)047<1205:IBUALT>2.0.CO;2

Skamarock, W. C., Klemp, J. B., Dudhia, J., Gill, D. O., Barker, D. M., Wang, W., & Powers, J. G. (2005). A description of the Advanced Research WRF version 2. NCAR Technical Note NCAR/TN-468+STR

Stephan, C. C., Alexander, M. J., Hedlin, M., de Groot-Hedlin, C. D., & Hoffmann, L. (2016). A case study on the far-field properties of propagating tropospheric gravity waves. *Monthly Weather Review*, *144*(8), 2947–2961. https://doi.org/10.1175/MWR-D-16-0054.1

Stobie, J. G., Einaudi, F., & Uccellini, L. W. (1983). A case study of gravity waves–convective storms interaction: 9 May 1979. *Journal of the Atmospheric Sciences*, *40*(12), 2804–2830. https://doi.org/10.1175/1520-0469(1983)040<2804:ACSOGW>2.0.CO;2

Su, T., & Zhai, G. (2017). The role of convectively generated gravity waves on convective initiation: A case study. *Monthly Weather Review*, *145*(1), 335–359. https://doi.org/10.1175/MWR-D-16-0196.1

Sun, Y. Q., & Zhang, F. (2016). Intrinsic versus practical limits of atmospheric predictability and the significance of the butterfly effect. *Journal of the Atmospheric Sciences*, *73*(3), 1419–1438. https://doi.org/10.1175/JAS-D-15-0142.1

Thompson, G., Field, P. R., Rasmussen, R. M., & Hall, W. D. (2008). Explicit forecasts of winter precipitation using an improved bulk microphysics scheme. Part II: Implementation of a new snow parameterization. *Monthly Weather Review*, *136*(12), 5095–5115. https://doi.org/10.1175/2008MWR2387.1

Tulich, S. N., & Mapes, B. E. (2008). Multiscale convective wave disturbances in the tropics: Insights from a two-dimensional cloud-resolving model. *Journal of the Atmospheric Sciences*, *65*(1), 140–155. https://doi.org/10.1175/2007JAS2353.1

Uccellini, L. W. (1975). A case study of apparent gravity wave initiation of severe convective storms. *Monthly Weather Review*, *103*(6), 497–513. https://doi.org/10.1175/1520-0493(1975)103<0497:ACSOAG>2.0.CO;2

Uccellini, L. W., & Koch, S. E. (1987). The synoptic setting and possible energy sources for mesoscale wave disturbances. *Monthly Weather Review*, *115*(3), 721–729. https://doi.org/10.1175/1520-0493(1987)115<0721:TSSAPE>2.0.CO;2

Wang, S., & Sobel, A. H. (2011). Response of convection to relative SST: Cloud-resolving simulations in 2D and 3D. *Journal of Geophysical Research*, *116*, D11119. https://doi.org/10.1029/2010JD015347

Wang, S., Sobel, A. H., & Kuang, Z. (2013). Cloud-resolving simulation of TOGA-COARE using parameterized large-scale dynamics. *Journal of Geophysical Research: Atmospheres*, *118*, 6290–6301. https://doi.org/10.1002/jgrd.50510

Wang, S., & Zhang, F. (2007). Sensitivity of mesoscale gravity waves to the baroclinicity of jet-front systems. *Monthly Weather Review*, *135*(2), 670–688. https://doi.org/10.1175/MWR3314.1

Wang, S., Zhang, F., & Snyder, C. (2009). Generation and propagation of inertial gravity waves from vortex dipoles and jets. *Journal of the Atmospheric Sciences*, *66*(5), 1294–1314. https://doi.org/10.1175/2008JAS2830.1

Wang, Y., Zhang, L., Peng, J., & Guan, J. (2018). Mesoscale gravity waves in the Mei-Yu front system. *Journal of the Atmospheric Sciences*, *75*(2), 587–609. https://doi.org/10.1175/JAS-D-17-0012.1

Wheeler, M., & Kiladis, G. N. (1999). Convectively coupled equatorial waves: Analysis of clouds and temperature in the wavenumber–frequency domain. *Journal of the Atmospheric Sciences*, *56*(3), 374–399. https://doi.org/10.1175/1520-0469(1999)056<0374:CCEWAO>2.0.CO;2

Wilson, J. W., Trier, S. B., Reif, D. W., Roberts, R. D., & Weckwerth, T. M. (2018). Nocturnal elevated convection initiation of the PECAN 4 July hailstorm. *Monthly Weather Review*, *146*(1), 243–262. https://doi.org/10.1175/MWR-D-17-0176.1

Zhang, F. (2004). Generation of mesoscale gravity waves in uppertropospheric jet–front systems. *Journal of the Atmospheric Sciences*, *61*(4), 440–457. https://doi.org/10.1175/1520-0469(2004)061<0440:GOMGWI>2.0.CO;2

Zhang, F., Bei, N., Rotunno, R., Snyder, C., & Epifanio, C. C. (2007). Mesoscale predictability of moist baroclinic waves: Convection-permitting experiments and multistage error growth dynamics. *Journal of the Atmospheric Sciences*, *64*(10), 3579–3594. https://doi.org/10.1175/JAS4028.1

Zhang, F., & Koch, S. E. (2000). Numerical simulations of a gravity wave event over CCOPE. Part II: Waves generated by an orographic density current. *Monthly Weather Review*, *128*(8), 2777–2796. https://doi.org/10.1175/1520-0493(2000)128<2777:NSOAGW>2.0.CO;2

Zhang, F., Koch, S. E., Davis, C. A., & Kaplan, M. L. (2001). Wavelet analysis and the governing dynamics of a large-amplitude mesoscale gravity-wave event along the East Coast of the United States. *Quarterly Journal of the Royal Meteorological Society*, *127*(577), 2209–2245. https://doi.org/10.1002/qj.49712757702

Zhang, F., Koch, S. E., & Kaplan, M. L. (2003). Numerical simulations of a large-amplitude mesoscale gravity wave event. *Meteorology and Atmospheric Physics*, *84*(3-4), 199–216. https://doi.org/10.1007/s00703-002-0594-2